Journal of Mines, Metals and Fuels, *72(8): 863-871; 2024. DOI: 10.18311/jmmf/2024/44870*

Print ISSN : 0022-2755

Journal of Mines, Metals and Fuels

Contents available at: *www.informaticsjournals.com/index.php/jmmf*

Bi^{3+} Co-Doped Multi-Metal Stack, $LaAlO_3:Dy^{3+}$Nano Perovskites: Performance and Efficiency Characteristics with Suitability for C-MOS Devices

Yashaswini[1], R. Venkatesh[1], Y. B. Vinaykumar[2], P. Shankar[3], S. R. Manohara[4], N. Sivasankara Reddy[5], N. Hanumantharaju[6] and A. Jayasheelan[6]*

[1]Centre for Advanced Materials Research Lab, Department of Physics, B.M.S. Institute of Technology and Management, Bangalore - 560064, Karnataka, India
[2]Department of Information Science and Engineering, B.M.S. Institute of Technology and Management, Bangalore - 560064, Karnataka, India
[3]Department of Physics, Sai Vidya Institute of Technology, Bangalore - 560064, Karnataka, India
[4]Nano-Composites and Materials Research Lab, Department of Physics, Siddaganga Institute of Technology, Tumakuru - 572103, Karnataka, India
[5]Department of Physics, Presidency University, Bangalore - 560004, Karnataka, India
[6]Department of Physics, Maharani Science College for Women, Bangalore - 560001, Karnataka, India; jayasheelanwillbe@gmail.com

Abstract

Perovskite $LaAlO_3$, $LaAlO_3:Dy^{3+}$ and $LaAlO_3:Dy^{3+}:Bi^{3+}$(1mol%) is a nano substance prepared through a chemical combustion process using sugar as a fuel. Powder X-ray Diffraction (PXRD) and Transmission Electron Microscopy (TEM) confirm an irregularly shaped non-polycrystalline nature with a Rhombohedral phase of space group R3m having crystallite size ranging between 24-26 nm. Scanning electron microscopy and energy dispersive spectra confirm the porous, dumbbell-shaped morphology and its constituents. The Fourier Transform Infrared (FTIR) spectra peaks between 840cm^{-1} to 400cm^{-1} proving the presence of metal oxide and a peak located at 1380.0cm^{-1} ascribed to carboxylate ions vibrational modes present in the studied sample. The dielectric studies show a higher and increased dielectric constant for doped and codoped samples than the host sample, hence it may be used as storage devices. Cole-Cole plots for conductivity studies show semicircles at high frequencies indicating the grain effect. There was a continuous increase in the radius of the semicircle of the Cole-Cole plot, for host, doped and codoped samples indicating the increase in the material's resistance. Therefore, the prepared material finds applications in devices like Complementary Metal Oxide Semiconductor (CMOS).

Keywords: *CMOS Devices, Dielectric, Perovskite, Solution Combustion*

1.0 Introduction

The very process of dielectric studies of nano-materials mainly depends on the defects created by introducing Rare-Earth (RE) elements as activators and sensitisers and enhancing the surface-to-volume ratio in the synthesis process[1]. RE ions in the host substance expand the range of uses for phosphor material. The properties

*Author for correspondence

of phosphors are heavily influenced by the dopants used. The Dy^{3+} ions cause transitions from the $^4F_{9/2}$ level to the H- levels, which produces green wavelength emission in the ion centres[2]. The electrical, electronic, optical and magnetic properties of synthesised materials depend on the presence of sensitisers, like bismuth, which alter the environment of host compounds by creating defects and variations in the concentration of charge carriers[3].

Lanthanum Aluminate ($LaAlO_3$) is one of the widely used host materials compared to other varieties of Nano Phosphors (NP) because it is an inorganic ceramic oxide, which is quite stable, transparent to electromagnetic waves to a wider range of frequencies and possesses multifunctional applications. These materials along with their dopant/dopant/defect centres, show potentiality in optical display systems[4]. The process of sample preparation determines the sample's morphology, such as particle size, particle distribution and agglomeration, surface area and so on. Nano-particles can be prepared in a variety of ways, but Solution Combustion Synthesis (SCS) is the most popular and efficient process due to its simplicity, adaptability, and low cost. SCS produces high-purity samples of the appropriate composition quickly, making it ideal for commercial scaled-up manufacturing. This method also allows one to change various settings without compromising the repeatability of the attributes[5,6]. The nature of the nano-particles generated is determined by the temperature, fuel type, fuel-to-oxidant material ratio etc.

Further, $LaAlO_3$ and its derived products find applications such as turbines, capacitors, superconductors in thin films etc[7]. The dielectric and optical properties of these properties enable it to be used in many practical applications[8]. The present study investigated the size, composition, morphology, luminescence, dielectric, and impedance properties of $LaAlO_3$, Dy^{3+} activated and Bi^{3+}codoped NPs produced by chemical combustion with sugar as fuel. Doped $LaAlO_3$ has a superior host matrix and allows dopants to operate as donors or sensitisers, resulting in improved optical property tweaking.

2. Methodology

Analytical grade $La(NO_3)_3 6H_2O$, $Al(NO_3)_3 9H_2O$, $Dy(NO_3)_3 H_2O$ and $Bi(NO_3)_3 H_2O$ were used to prepare lanthanum aluminate using sugar as fuel by SCS method[9]. The ratio of oxidising agent (O) to fuel (F) was preserved at unity[10]. Undoped lanthanum aluminate was first synthesised by taking stoichiometric amounts of lanthanum nitrate and aluminium nitrate in a petri dish. The precursors were liquefied in purified water and heated in a sand bath for 10-15 minutes until they reached a gel consistency. Then, dopant/co-dopant and fuel were added to the gel. The solution was agitated for 20 minutes before being transferred to a preheated furnace (about 300 °C). The combination underwent dehydration, followed by a breakdown with the emission of several gases. After combustion, the product was calcined in the furnace for 3 hours at 900°C. The same procedures were repeated to prepare $LaAlO_3$:Dy^{3+} and $LaAlO_3$:Dy^{3+}:Bi^{3+} NPs.

2.1 Characterisation Methods Used

Powder X-ray Diffraction (PXRD) with Copper K_α radiation (1.54180 Å) was used to investigate the sample's size and phase. The band gap was evaluated using a Diffuse Reflectance Spectrophotometer (DRS) (300 for UV/Vis) with barium sulphate in the 200-1100 nm range. The produced sample's purity was investigated using a Perkin Elmer with spectrum-1000, FTIR spectrometer (350-4000 cm^{-1}) and KBR pellets. The morphology was studied using a Hitachi (TM 3000) Scanning Electron Microscope (SEM). The crystal's size and composition were estimated using TEM and JEOL, JEM-2100 microscope. Dielectric and impedance studies were carried out using an LCR (HIOKI-IM3536 model) meter in the range of 100Hz to 8MHz at ambient temperature.

3.0 Results and Discussions

3.1 Size, Shape, and Composition of Lanthanum Luminate NPs

Crystal structure, strain and average crystallite size of the prepared samples were examined using PXRD spectra as indicated in Figure 1(a). The diffraction pattern corroborated the rhombohedral phase, with space group R3m and lattice parameter a = 5.357 Å, after comparing with Joint Committee on Powder Diffraction Standards (JCPDS) file no. 85-1071. Using the Scherer formula, the average crystal size was determined.

$$D = \frac{k\lambda}{\beta Cos\theta} \quad (1)$$

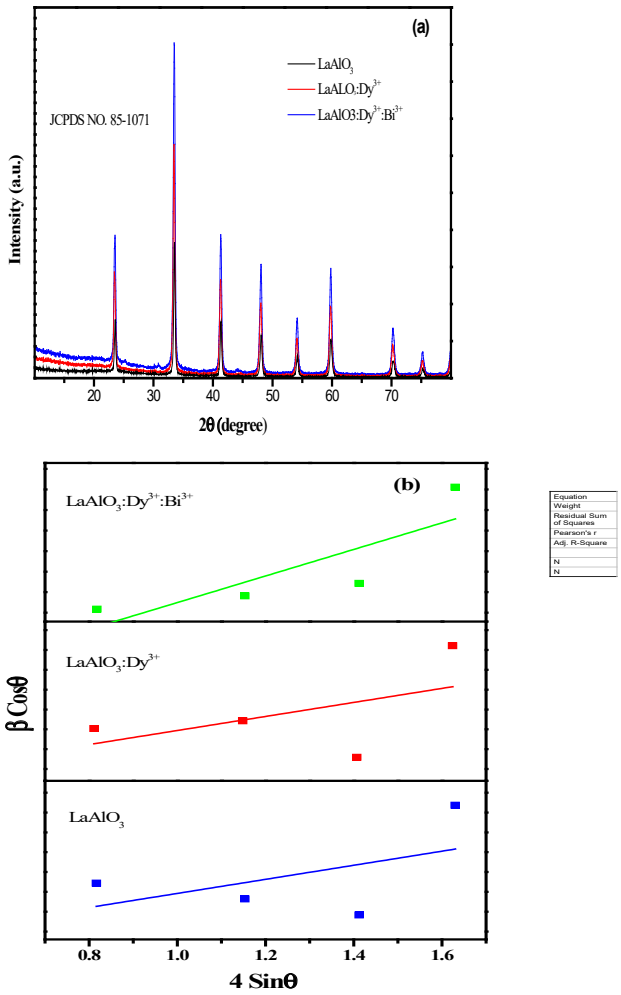

Figure 1. **(a)** PXRD diffraction pattern.**(b)** W-H analysis of lanthanum aluminate NPs.

Crystal diameters ranged between 24-26 nm. The drop in size for the doped/co-doped samples was caused by flaws in the sample as a result of Dy^{3+}'s reduced ionic radius (91pm) compared to lanthanum's (122pm). The addition of Dy^{3+} to the host matrix replaces La ions in the structure and introduces defects that promote orbital contraction, resulting in higher orbital density. The crystal sizes were also estimated using the Williamson-Hall ratio, which connects strain and angle of diffraction. Stokes and Wilson's method confirmed the strain in the material[11].

$$\varepsilon = \frac{\beta}{4tan\theta} \qquad (2)$$

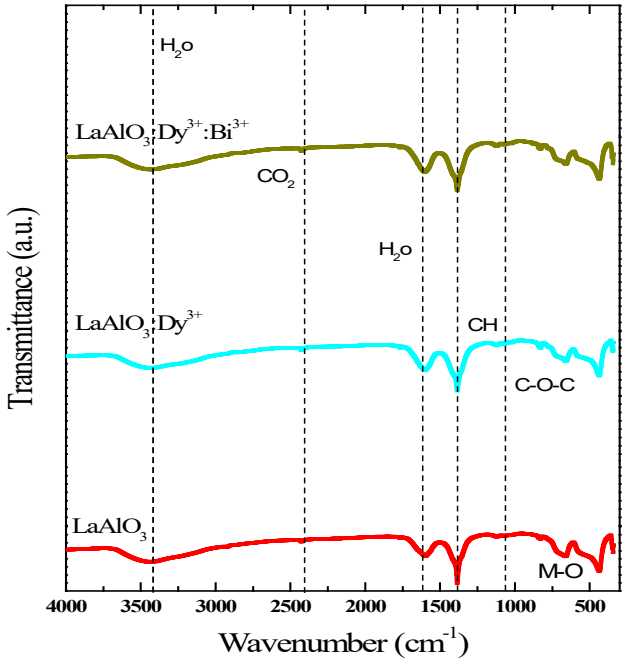

Figure 2. FTIR spectra of lanthanum aluminate NPs.

$$\beta Cos\theta = \frac{k\lambda}{D} + 4\,\varepsilon\,Sin\theta \qquad (3)$$

In the above expression, 'D' is the mean crystallite size. The slope of the graph'β Cosθ' against '4 Sinθ', gives strain (ε) and intercept ((0.9λ)/D) indicates the size of the crystals (Figure 1(b)). The mean crystallite size from this analysis was found to be in the range of 32-36nm. The variation in the sizes between the Scherer method and the W-H method is due to the consideration of strain to be zero. FTIR spectra were used for the determination of the nature of chemical bonding, shown in Figure 2. A broad spectral band was found by the absorption of ~ 3400.0cm^{-1} and ~1602.0cm^{-1}, confirming hydroxyl ions[12]. The sharp peak at 2431.0cm^{-1} is absorbed by CO_2 molecules[13]. The spectral peak of about 1380cm^{-1} may be linked to the vibrational modes of the carboxylate ions. Further, the specific peaks at 426cm^{-1}, 677.0cm^{-1} and 825.0cm^{-1}in the range 840.0cm^{-1} to 400.0cm^{-1} would be accredited to the oxide metal bonding[14] in the prepared sample.

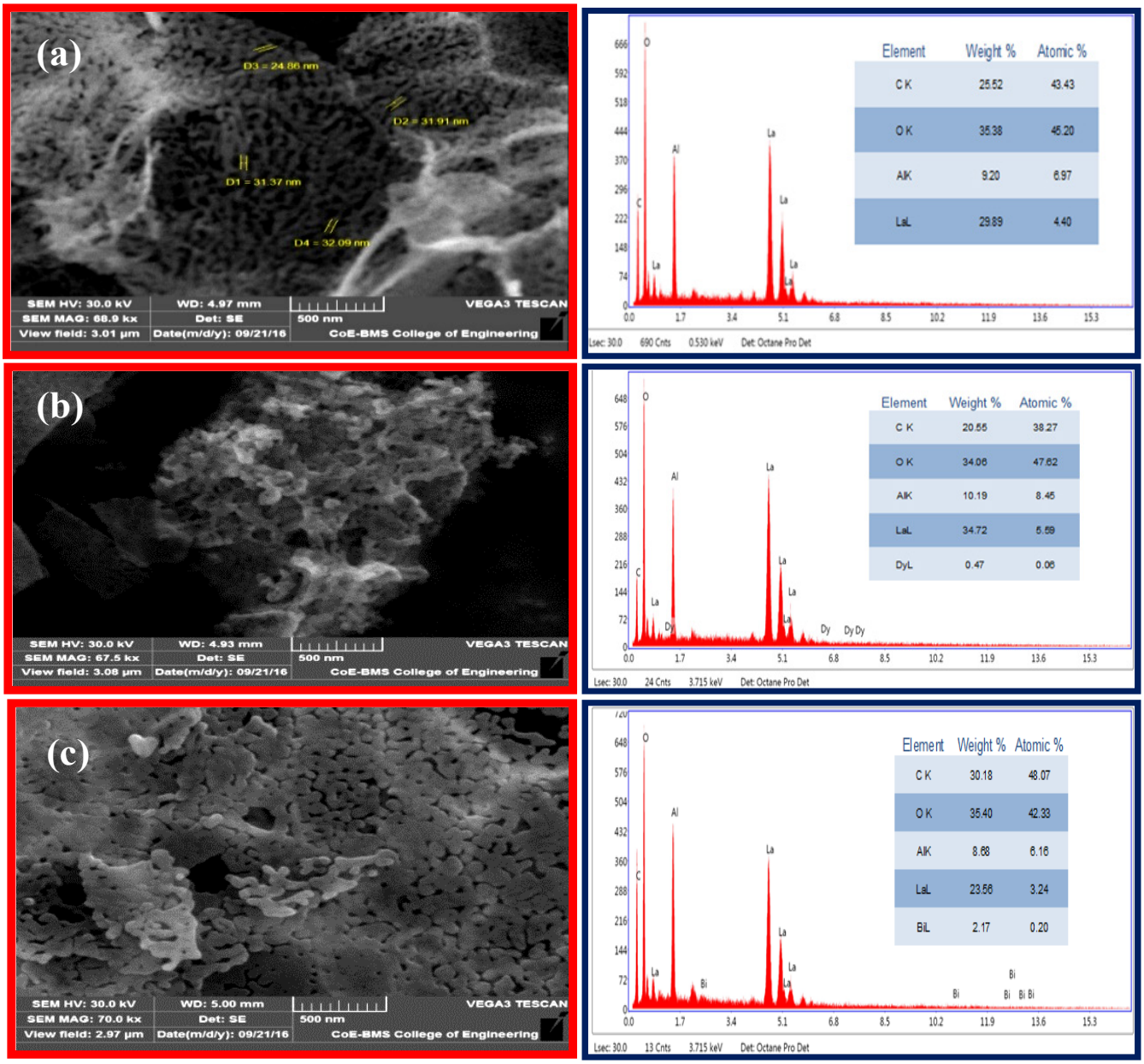

Figure 3. SEM images attached with EDS spectra of (**a**) $LaAlO_3$ (**b**) $LaAlO_3$:Dy^{3+}. (**c**) $LaAlO_3$:Dy^{3+}:Bi^{3+} NPs.

The morphology and surface features have a significant impact on the properties of nanostructures. Figure 3, displays the morphology and Energy Dispersive Spectra (EDS) gives the constituents present in the sample. The SEM micrographs reveal the porous, agglomerated, dumbbell-shaped structure and reduced size of the particles when the host material is doped. The decrease in the particle size is due to the modification in the structure of the host lattice. The presence of carbon content in all samples evidenced by EDS was due to the use of carbon tape while taking SEM analysis.

Actual size was also verified using TEM images for Dy^{3+} (1 mol %) activated $LaAlO_3$ sample and shown in Figure 4. Figure 4(a) is a dark field image with a bright

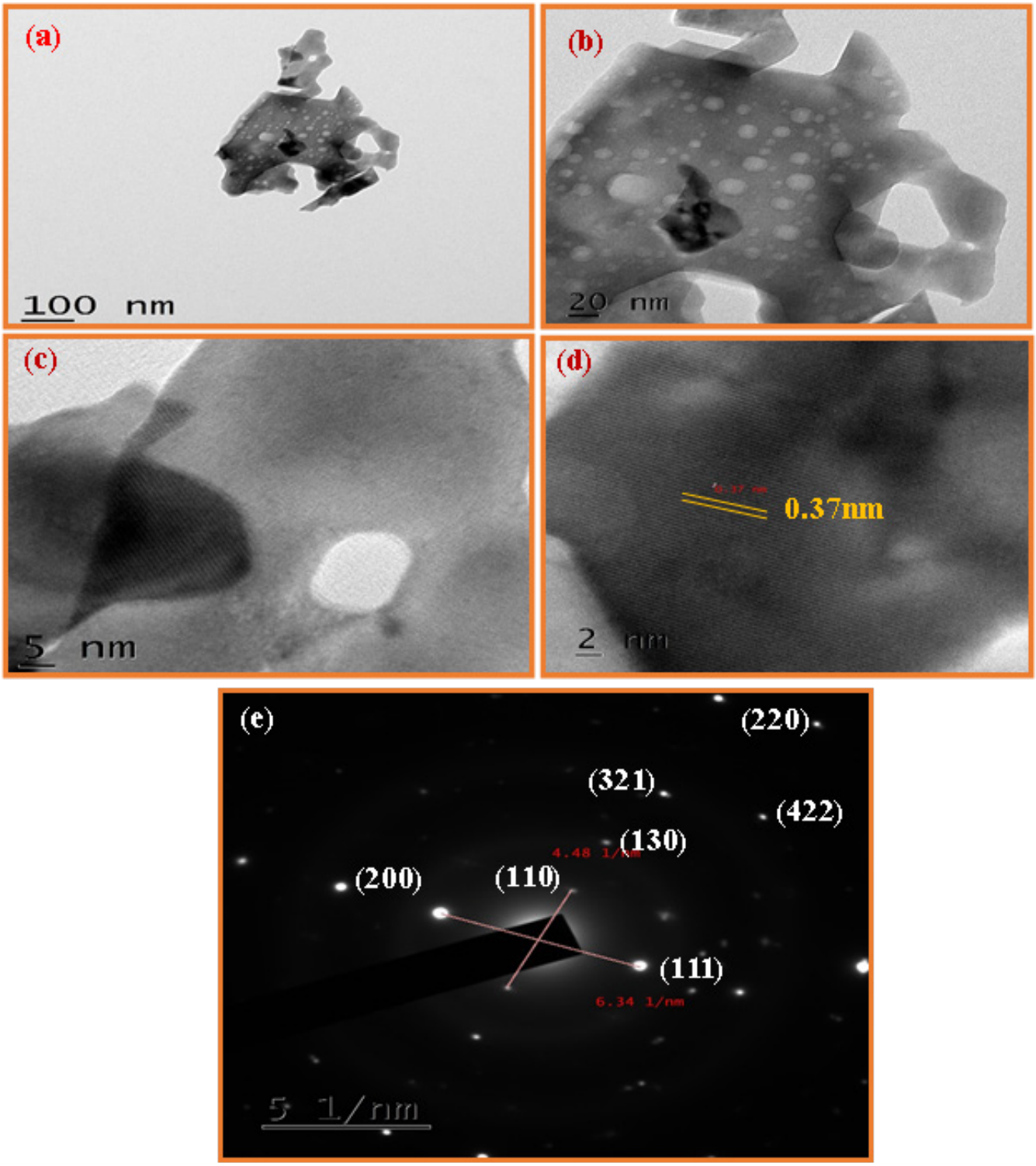

Figure 4. TEM images of the Dy^{3+}-doped lanthanum aluminate sample (**a**) High-angle annular dark field (HAADF) image. (**b**) enlarged image of HAADF. (**c**) Bright field (BF) images. (**d**) Brags lines of the sample (**e**) SAED image.

background showing individual dumbbell-shaped structures of NPs having a size of about 65nm and was matched with PXRD analysis. Figure 4(b) gives the image of the sample with high resolution for the selected area. It can be observed that the clear atomic planes were observed and inter-planar spacing of about 3.7Å for the (hkl) plane of (111) was estimated and the same was co-related by PXRD analysis. The irregular-shaped non-poly-crystalline sample was confirmed by the Selected Area Electron Diffraction (SAED) pattern which was shown in Figure 4(e).

Optical band gap energy can be calculated for any solid material by diffuse reflectance UV-Vis spectroscopy. The energy gap, E_g, is found by the Kubelka-Munk (K-M) method for the synthesised NPs using optical reflection spectra is shown in Figure 5. F(R) was determined by the expression

$$F(R_\infty) = \frac{(1-R_\infty)^2}{2R_\infty} \quad (4)$$

In the above relation, R is reflectance and F(R) is K-M which directly depends on the coefficient of absorption.

$$h\nu = \frac{1240}{\lambda} \quad (5)$$

'E_g'values calculated by the K-M model were in the range of 2.75-3.0 eV resulting in the insulating nature of the samples. From Figure 5, it was confirmed that the energy band gap of the host material is lower than that of the doped material and that of the co-doped material. This might be due to the existence of defects in the prepared nanomaterials due to the effect of doping or co-doping.

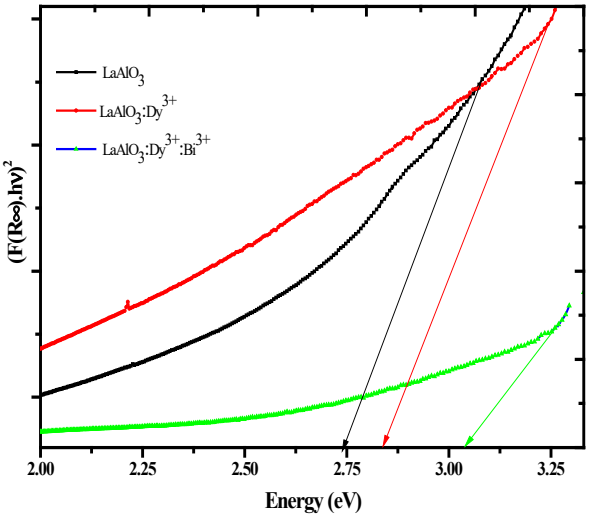

Figure 5. Optical reflection spectra of lanthanum aluminate NPs.

3.2 Dielectric Properties of Lanthanum Aluminate NPs

Relative permittivity's real part indicates how much information has been retained in the dielectric sample,

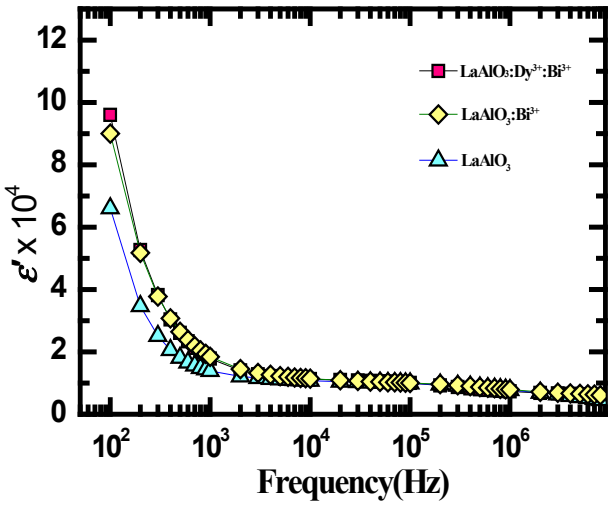

Figure 6. Real part of dielectric constant of lanthanum aluminate NPs for various frequency at room temperature.

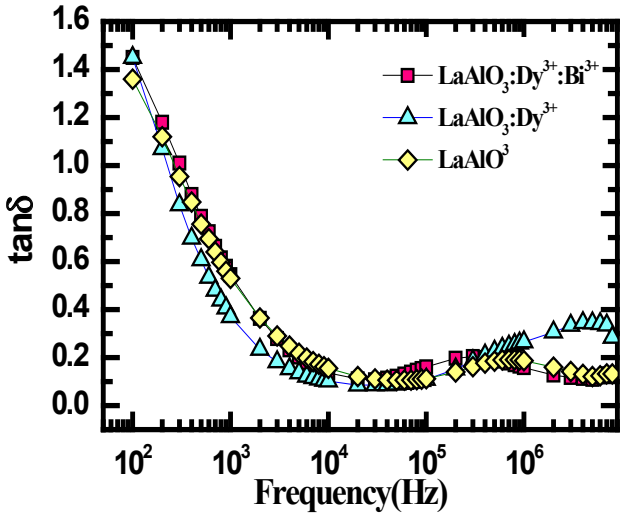

Figure 6. Dielectric loss verses frequency of lanthanum aluminate NPs for various frequency at room temperature.

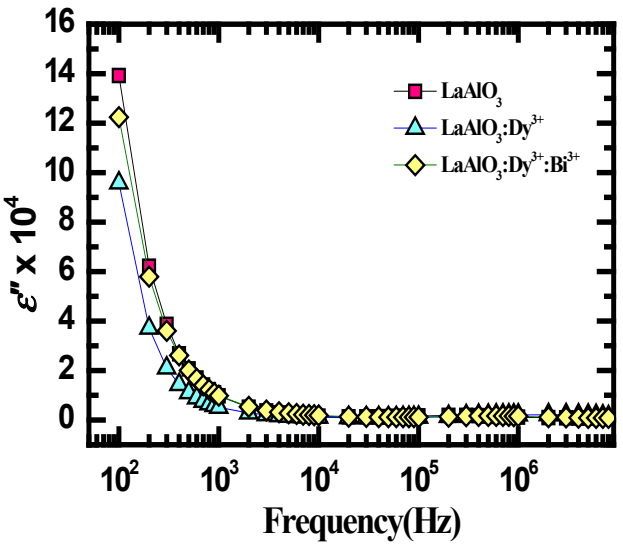

Figure 8. Imaginary part of dielectric constant of lanthanum aluminate NPs for various frequency at room temperature.

while its imaginary part indicates how much energy is lost through the material.

The dielectric constant, ε' (real part), was determined by the expression

$$\varepsilon' = \frac{\varepsilon}{\varepsilon_0} \qquad (6)$$

Where, ε_0 is the permittivity of free space, a constant, ε is absolute permittivity. The frequency studies (100Hz -8MHz) of ε' for the present NPs at Room Temperature (RT) are shown in Figure 6. It was observed that, as the frequency was raised, ε' lowered and reached the lowest value. The carriers of charge cannot align along the applied field direction, thereby reducing ε'[15]. The loss of energy in the form of heat is caused due to resonance in the domain wall as frequency increases at RT, which is nothing but the dielectric loss (Figure 7). The change in rotation of the domain, due to the motion of the domain wall caused by the magnetisation of the sample at high frequencies

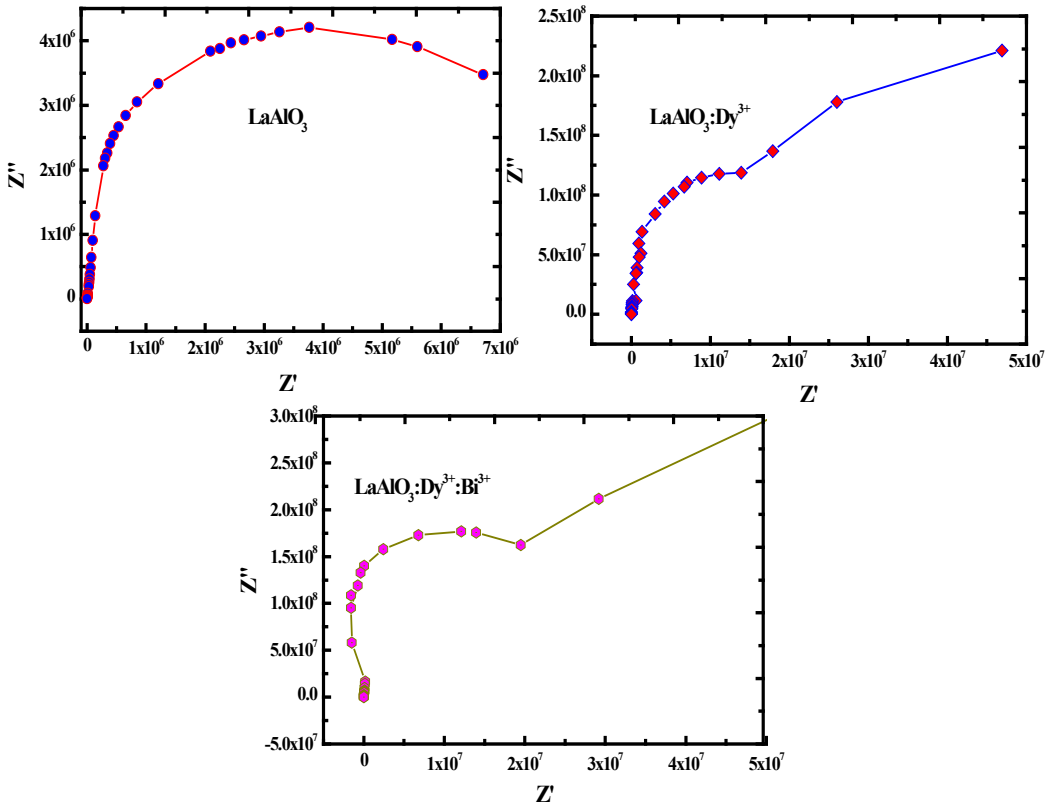

Figure 9. Nyquist diagram (Cole-Cole plot) of lanthanum aluminate NPs.

produces low dielectric loss. The measured higher value dielectric loss at low frequency is due to relaxation time by the jumping localised charge carriers[16]. High loss at low-frequency regions was owing to grain boundary confinements. Since the loss is low at high frequency, they find applications at high frequency. Figure 8 shows, the graph of frequency and ε″(imaginary part) calculated from Expression (7).

$$\varepsilon'' = \tan\delta \times \varepsilon_0 \quad (7)$$

Many phenomena such as grain boundary defect, polarisation, O_2 vacancies etc. are responsible for the reduction of ε″ when frequency is increased[17]. This can also be justified using the Maxwell-Wagner homogeneous model (MW model)[18]. As per this model, the polarisation attains a fixed value after decreasing due to jumping charge carriers till some frequency after this frequency jumping between metal ions (La, Dy and Al) fails to align to the external field. In the present study, a decrease in ε″ with increasing frequency was observed, which may be due to the friction between dipoles causing loss of heat energy called dielectric loss. Therefore, the dielectric loss is less at greater frequencies. At this frequency, ionic polarisations and dipoles align in field directions immediately thereby reducing the friction and causing a decrease of ε″ and tanδ.

An impedance study can be employed to analyse the contribution of conductivity for both ε' and ε″ when an external AC field is applied[19]. Nyquist diagram or Cole-Cole plot is shown in Figure 9. From the graph, it can be concluded that the appearance of semicircles in the entire sample signifies the relaxation process and its radius is a direct measure of resistance of the material[20]. The presence of a semicircular graph at a high-frequency range may be due to the grain effect and the depressed semicircle which appeared for the doped and co-doped samples showed an increase in the radius of the semicircle indicating the rise in resistance of the material for frequency-ranging between 100Hz to 8MHz.

4.0 Conclusion

Morphological, optical and dielectric properties of undoped and doped $LaAlO_3$ perovskites prepared by SC method using sugar as a fuel were determined. PXRD and TEM analysis of the prepared samples confirm polycrystalline nature with crystallite size in the range of 24-26nm showing rhombohedral structure agreeing with JCPDS No. 85-1071. SEM images confirm irregular and spherical clustered morphology with pale areas resembling higher atomic numbers and hollow structures. FTIR spectra show sharp peaks between 750–400 cm^{-1} corresponding to metal oxide (M–O) (M=La and/or Al) characteristic bonds. The band gap was determined using DRS spectra around 2.75 to 3.0 eV. The energy gap of host material < doped material < co-doped material. Thus, the study confirmed that an increase in dopant concentration increases the optical band gap.

The dielectric constant showed the usual trend, i.e., a fall with a rise in frequency. This was due to a decrease in polarisation. At higher frequencies, it exhibited a low and constant value. The fall in 'tan δ' when the frequency rises shows dispersion behaviour. Impedance analysis using the Cole-Cole plot showed semicircles in the plot, where the radius of the semicircle decreased with the addition of dopant and co-dopant to the host material indicating the decrease in resistance of the prepared sample. This behaviour is suitable for manufacturing frequency meter applications as the loss is high at low applied frequencies.

5.0 Acknowledgements

One of the authors Dr Yashaswini acknowledges the Management and Principal, BMSIT and M for their constant support and encouragement. The corresponding author extends gratitude to Vision Group of Science and Technology (VGST), Government of Karnataka.

6.0 Data Availability

The data required to reproduce these findings are available from the corresponding authors upon reasonable request.

7.0 References

1. Venkatesh R, Dhananjaya N, Sateesh MK, Begum JPS, Yashodha SR. Effect of Li, Na, K cations on photoluminescence of $GdAlO_3$: Eu^{3+} nanophosphor and study of Li cation on its antimicrobial activity. J Alloys and Comp. 2018; 732:725-39. https://doi.org/10.1016/j.jallcom.2017.10.117
2. Singh VS, Watanabe S, Gundu Rao TK, Chubaci JFD, Ho-Young Kwak. Characterization, photoluminescence,

thermally stimulated luminescence and electron spin resonance studies of Eu^{3+} doped $LaAlO_3$ phosphor. Sol State Sci. 2011; 13(1):66-71. https://doi.org/10.1016/j.solidstatesciences.2010.10.010

3. Zhereb VP, Skorikov VM. Metastable states in bismuth-containing oxide systems. Inorg Mater. 2003; 39:S121-S45. https://doi.org/10.1023/B:INMA.0000008890.41755.90
4. Hemasundara Raju S, Thyagarajan K, Sudhakar Reddy B, Nageswara Raju C. Synthesis process and luminescence properties of Pr^{3+}: $BaGd_2Ti_4O1_2$ ceramics. Mat Today Proc. 2015; 2:4463-7. https://doi.org/10.1016/j.matpr.2015.10.050
5. Chandradass J, Kim KH. Mixture of fuels approach for the solution combustion synthesis of $LaAlO_3$ nanopowders. Adv Powd Tech. 2010; 21:100-5. https://doi.org/10.1016/j.apt.2009.10.014
6. Aruna ST, Kini NS, Rajam KS. Solution combustion synthesis of CeO_2-$CeAlO_3$ nano-composites by mixture-of-fuels approach. Mater Res Bull. 2009; 44:728-33. https://doi.org/10.1016/j.materresbull.2008.09.034
7. Guo R, Guo D, Chen Y, Yang Z, Yuan Q. Ceram. In situ formation of LaAl11O18 rod-like particles in ZTA ceramics and effect on the mechanical properties. Int. 2002; 28:699-704. https://doi.org/10.1016/S0272-8842(02)00031-7
8. Zylberberg J, Yea Z. Improved dielectric properties of bismuth-doped $LaAlO_3$. J Appl Phys. 2006; 100:086102-3. https://doi.org/10.1063/1.2358827
9. Wal A, Wal P, Gupta N, Vishnoi G, Srivastava. Medicinal value of Euphorbia tirucalli. Int J Pharm and Bio Arch. 2013; 4:31-40. https://doi.org/10.4103/0975-8453.135843
10. Chandradass J, Kim KH. Synthesis and characterization of $LaAlO_3$ nanopowders by emulsion combustion method. J Alloys and Comp. 2009; 481:131-4. https://doi.org/10.1016/j.jallcom.2009.03.072
11. Reimann K, Würschum R. Distribution of internal strains in nanocrystalline Pd studied by x-ray diffraction. J Appl Phy. 1997; 81:7186. https://doi.org/10.1063/1.365307
12. Barabauskas A, Jasaitis D, Kareiva A, Characterization of sol-gel process in the Y-Ba-Cu-O acetate-tartrate system using IR spectroscopy. Vib Spect. 2002; 28:263-75. https://doi.org/10.1016/S0924-2031(01)00157-6
13. Socrates G, Infrared and raman characteristic group frequencies tables and charts, third ed., Chichester, Wiley; 2001.
14. Schrader B, Infrared raman spectroscopy: Methods and applications, VCH, Weinheim, 1995. https://doi.org/10.1002/9783527615438
15. Abbas S, Munir A, Zahra F, Rehman MA. Enhanced electrical properties in Nd-doped cobalt ferrite nanoparticles. Mat Sci and Engg. 2016; 146:012027. https://doi.org/10.1088/1757-899X/146/1/012027
16. Abdeen AM, Hemeda OM, Assem EE, El-Sehly MM. Structural, electrical and transport phenomena of co-ferrite substituted by Cd. J Mag Mag Mat. 2002; 238:75-83. https://doi.org/10.1016/S0304-8853(01)00465-6
17. Vasoya NH, Lakhani VK, Sharma PU, Modi KB, Ravi Kumar, Joshi HH. Study on the electrical and dielectric behaviour of Zn-substituted cobalt ferrialuminates. J Phys Cond Matt. 2006; 18:8063-92. https://doi.org/10.1088/0953-8984/18/34/017
18. Xavier S, Thankachan S, Jacob BP, Mohammed EM. International conference on material science and technology (ICMST 2012), Mat Sci Engg. 2015; 73:012093. https://doi.org/10.1088/1757-899X/73/1/012093
19. Farea AM, Kumar S, Batoo KM, Yousef A, Lee CG, Structure and electrical properties of Co0. 5CdxFe2. 5–xO4 ferrites. J Alloys Comp. 2008; 464:361-9. https://doi.org/10.1016/j.jallcom.2007.09.126
20. Irvine JT, Sinclair DC, West AR, Electroceramics: characterization by impedance spectroscopy. Adv Mat. 1990; 2:132-8. https://doi.org/10.1002/adma.19900020304